CrossMark

CAMBRIDGE
UNIVERSITY PRESS

Research Paper

The Rapid ASKAP Continuum Survey I: Design and first results

D. McConnell[1], C. L. Hale[2], E. Lenc[1], J. K. Banfield[1], George Heald[2], A. W. Hotan[2], James K. Leung[1,3], Vanessa A. Moss[1], Tara Murphy[3], Andrew O'Brien[1,4,5], Joshua Pritchard[1,3], Wasim Raja[1], Elaine M. Sadler[1,3], Adam Stewart[3], Alec J. M. Thomson[2], M. Whiting[1], James R. Allison[6], S. W. Amy[1], C. Anderson[2,7], Lewis Ball[1,8], Keith W. Bannister[1], Martin Bell[1,9], Douglas C.-J. Bock[1], Russ Bolton[1], J. D. Bunton[1], A. P. Chippendale[1], J. D. Collier[1,5,10], F. R. Cooray[1], T. J. Cornwell[1,11], P. J. Diamond[1,8], P. G. Edwards[1], N. Gupta[1,12], Douglas B. Hayman[1], Ian Heywood[6,13], C. A. Jackson[1,14], Bärbel S. Koribalski[1], Karen Lee-Waddell[1], N. M. McClure-Griffiths[15], Alan Ng[1], Ray P. Norris[1,5], Chris Phillips[1], John E. Reynolds[1], Daniel N. Roxby[1], Antony E. T. Schinckel[1], Matt Shields[1], Chenoa Tremblay[2], A. Tzioumis[1], M. A. Voronkov[1] and Tobias Westmeier[16]

[1]CSIRO Astronomy and Space Science, PO Box 76, Epping, NSW 1710 Australia, [2]CSIRO Astronomy and Space Science, PO Box 1130, Bentley, WA 6102, Australia, [3]Sydney Institute for Astronomy, School of Physics, University of Sydney, Sydney, NSW 2006, Australia, [4]Center for Gravitation, Cosmology, and Astrophysics, Department of Physics, University of Wisconsin-Milwaukee, Milwaukee, WI 53201, USA, [5]Western Sydney University, Locked Bag 1797, Penrith, NSW 2751, Australia, [6]Sub-dept of Astrophysics, Physics, University of Oxford, Denys Wilkinson Building, Keble Road, Oxford, OX1 3RH, UK, [7]Jansky fellow of the National Radio Astronomy Observatory, NRAO, 1003 Lopezville Rd, Socorro, NM 87801 USA, [8]SKA Organisation, Jodrell Bank, Lower Withington, Macclesfield, Cheshire SK11 9FT, UK, [9]University of Technology Sydney, 15 Broadway, Ultimo, NSW 2007, Australia, [10]Department of Astronomy, The Inter-University Institute for Data Intensive Astronomy (IDIA), University of Cape Town, Private Bag X3, Rondebosch, 7701, South Africa, [11]Tim Cornwell Consulting, 17 Elgan Crescent, Sandbach CW111LD, UK, [12]Inter-University Centre for Astronomy and Astrophysics, Post Bag 4, Ganeshkhind, Pune 411007, India, [13]Department of Physics & Electronics, Rhodes University, Makhanda, 6140, South Africa, [14]ASTRON, The Netherlands Institute for Radio Astronomy, Oude Hoogeveensdijk 4, Dwingeloo 7991 PD, Netherlands, [15]Research School of Astronomy & Astrophysics, Australian National University, Canberra 2611, Australia and [16]ICRAR, M468, The University of Western Australia, 35 Stirling Hwy, Crawley, WA 6009, Australia

Abstract

The Rapid ASKAP Continuum Survey (RACS) is the first large-area survey to be conducted with the full 36-antenna Australian Square Kilometre Array Pathfinder (ASKAP) telescope. RACS will provide a shallow model of the ASKAP sky that will aid the calibration of future deep ASKAP surveys. RACS will cover the whole sky visible from the ASKAP site in Western Australia and will cover the full ASKAP band of 700–1800 MHz. The RACS images are generally deeper than the existing NRAO VLA Sky Survey and Sydney University Molonglo Sky Survey radio surveys and have better spatial resolution. All RACS survey products will be public, including radio images (with ~ 15 arcsec resolution) and catalogues of about three million source components with spectral index and polarisation information. In this paper, we present a description of the RACS survey and the first data release of 903 images covering the sky south of declination $+41°$ made over a 288-MHz band centred at 887.5 MHz.

Keywords: radio continuum: general – surveys

(Received 31 July 2020; revised 6 October 2020; accepted 12 October 2020)

1. Introduction

The Rapid ASKAP Continuum Survey (RACS) is a shallow all-sky precursor to the full, multi-year surveys to be conducted with the Australian SKA[a] Pathfinder (ASKAP; Johnston et al. 2007; Hotan et al. submitted). It will image the entire sky south of declination

[a]Square Kilometre Array.

$\delta = +51°$ over representative bands within ASKAP's operating frequency range of 700–1800 MHz. The aims of this survey are to generate reference images to aid ASKAP's future operation, to exercise the newly commissioned instrument ahead of the commencement of its full scientific operations and to provide a valuable astronomical resource.

ASKAP was designed to be a survey instrument capable of quickly observing the whole accessible sky. It is located at the Murchison Radio-astronomy Observatory (MRO) in Western Australia and is operated by the Commonwealth Scientific and Industrial Research Organisation (CSIRO). ASKAP is an array of 36 12-m prime focus antennas; each is equipped with a phased array feed (PAF) that enables the simultaneous digital formation of 36 dual-polarisation beams to sample its 31 deg^2 field of view. It has an instantaneous bandwidth of 288 MHz. A full description of ASKAP is in preparation (Hotan et al. submitted), but

Table 1. Summary of RACS parameters with those of other comparable surveys. The tabulated data allow comparison with RACS; for detailed information consult the reference papers mentioned in Section 1.

Survey	Frequency (MHz)	Bandwidth (MHz)	Resolution (arcsec)	Sky coverage (deg^2)	Sensitivity (mJy beam^{-1})	Polarization	$N_{sources}$ ($\times 10^6$)
VLSSr	73.8	3.12	75	30 793	100	*I*	0.93
GLEAM	87, 118, 154, 185, 215	30.72	120	27 691	6–10	*I, Q, U, V*	0.33
TGSS	150	16.7	25	36 900	2–5	*I*	0.62
RACS ^{a}	887.5 1 295.5 1 655.5	288	15	36 656	∼0.25	*I, Q, U, V*	4
RACS ^{b}	887.5	288	15–25	34 240	0.2–0.4	*I*	2.8
SUMSS +MGPS-2	843	3	45	10 300	1.5	RC	0.2
NVSS	1 346, 1 435	42	45	33 800	0.45	*I, Q, U*	2
VLASS	3 000	2 000	2.5	33 885	0.07	*I, Q, U*	5.3

^{a} RACS full survey capability.
^{b} RACS first data release.

descriptions of the PAFs, beam formation, and telescope operation exist in Hotan et al. (2014) and McConnell et al. (2016).

The data gathering capacity of ASKAP, equal to 36 simultaneous 630-baseline synthesis arrays, presented a software development challenge: how to develop calibration and imaging software that could run in less time than the time taken to make the observations. In addition to the use of highly parallel supercomputers, the solution relied upon the availability of a model of the sky that could provide the properties of all the major sources in any field being observed (Cornwell et al. 2011b). The aim was to construct this model [the Global Sky Model (GSM)] from short observations made with ASKAP itself, and that all subsequent observations would contribute to its improvement. Although the early operation of ASKAP makes no attempt to form images in real time, the availability of a sky model will assist data calibration and reduce reliance on time-consuming observations of calibration sources. The survey we describe here will allow the initialisation of the GSM.

RACS will be a valuable resource and will complement other all-sky radio surveys. Table 1 gives a comparison of the RACS survey parameters with other comparable radio surveys with substantial Southern-sky coverage in the metric and decimetric bands: Very Large Array Low-frequency Sky Survey Redux (VLSSr; Lane et al. 2014), Galactic and Extragalactic All-sky Murchison Widefield Array survey (GLEAM; Wayth et al. 2015; Hurley-Walker et al. 2017; Lenc et al. 2018), TIFR GMRT Sky Survey (TGSS-ADR1; Intema et al. 2017), NRAO VLA Sky Survey (NVSS; Condon et al. 1998), Sydney University Molonglo Sky Survey (SUMSS; Mauch et al. 2003), Molonglo Galactic Plane Survey (MGPS-2; Murphy et al. 2007), and the VLA Sky Survey (VLASS; Lacy et al. 2020). Together, NVSS in the north and SUMSS and MGPS-2 in the south cover the whole sky and have been the primary reference for radio sources at gigahertz frequencies. It is clear from Table 1 that RACS fills a critical niche connecting low-frequency surveys at metre wavelength to existing and forthcoming decimetric surveys. Sensitive wideband coverage in this intermediate regime strengthens efforts to understand the broadband spectra of the radio source population (e.g., Callingham et al. 2017; de Gasperin, Intema, & Frail 2018). RACS also establishes

a solid reference catalogue against which to assess radio source variability and transient candidates as future surveys emerge from ASKAP, MeerKAT, and the SKA.

This paper is a companion to the first RACS data release of 903 images made at a centre frequency of 887.5 MHz and covering the sky south of $\delta = +41°$ (83% of the celestial sphere). We outline the survey design in Section 2 and how it uses the established capabilities of the telescope. In Section 3, we describe the specific approach taken with the first epoch of observations and present their results. We discuss image quality and describe some extra steps taken to optimise the scientific utility of the RACS data products. Section 4 lists the products to be released and gives some examples of RACS images. In Section 5, we summarise the the current state of the survey and our plans for its future.

2. Survey design

RACS observations cover the whole accessible sky over representative portions of ASKAP's operating frequency range. Each observation is made with the telescope's full instantaneous bandwidth of 288 MHz, divided into 288 contiguous frequency channels. To reach the RACS point-source detection sensitivity goal of approximately 1 mJy, an integration time of ∼1 000 s per pointing is needed. All four polarisation products (XX, XY, YX, and YY) are recorded to allow images to be made in Stokes parameters *I*, *Q*, *U*, and *V*. The data are processed on the facilities of the Pawsey Supercomputing Centre using the ASKAPsoft software package (Cornwell et al. 2011a), and images are made available on the CSIRO ASKAP Science Data Archive[b] (CASDA; Chapman et al. 2017).

A catalogue of total intensity source components identified in RACS images is being constructed and will be described in the second paper, 'paper II' (Hale et al. in preparation) and will be released on CASDA. The calibrated RACS data are also being used to prepare frequency-resolved images in linear polarisation that will yield a catalogue of rotation measures across the survey area (Thomson et al. in preparation).
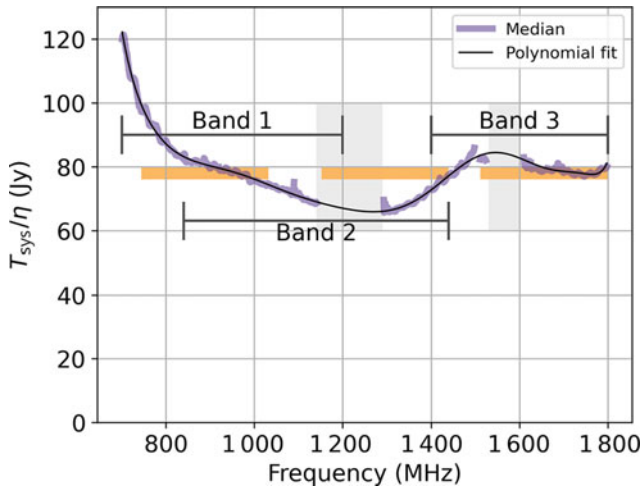
[b]https://research.csiro.au/casda/.

Figure 1. ASKAP sensitivity over its frequency range. The purple line traces the median value of central beams of all 36 antennas. Bands affected by radio-frequency interference are shaded grey. ASKAP's three tuning ranges are shown and labelled. The proposed RACS bands are shown as orange bars.

2.1. Spectral coverage

The full spectral coverage of ASKAP spans 700–1800 MHz; however, each observation is restricted to a contiguous 288 MHz band within that range. The choice of observing band has constraints based on both hardware and the presence of airborne and orbiting sources of radio-frequency interference (RFI). Figure 1 shows the proposed RACS frequency coverage. The first RACS data were collected over the 288-MHz wideband centred at 887.5 MHz. Subsequent RACS observations will be tuned to centre frequencies of 1 295.5 and 1 655.5 MHz; however, parts of these bands will be severely affected by RFI.

2.2. Field of view

ASKAP's field of view is approximately square. Sensitivity measurements across the field of view show that its shape is in good agreement with the predictions of modelling by Bunton & Hay (2010), and that it has an equivalent area of 31 deg^2, independent of frequency. Note that the full field of view cannot be sampled at the shorter wavelengths with the 36 beams available (Hotan et al. submitted).

Beams are formed to lie within the field of view, giving sensitivity to sky emission over a tile[c] of area $\leq$31 deg^2 (Figure 2). The size of each tile is determined by the beam pattern (footprint) and beam spacing. The choice of beam spacing is driven by several factors and depends on the scientific goals.

Survey speed varies in proportion to

$$\int_{\Theta} \frac{1}{\sigma^2(\theta, \phi)} d\theta \, d\phi, \qquad (1)$$

where $\sigma^2(\theta, \phi)$ is the system noise variance over the tile; θ and ϕ are orthogonal angular coordinates over the solid angle Θ subtended by the tile. Random noise is partially correlated between adjacent beams (because of their shared use of adjacent

---

[c]We use three terms for similar, but not identical concepts: a 'mosaic' is any image formed by linear combination of another set of (usually) overlapping images; a 'footprint' is the arrangement and distribution of electronically formed beams within the field of view; and a 'tile' is the patch of sky imaged in a single ASKAP pointing.
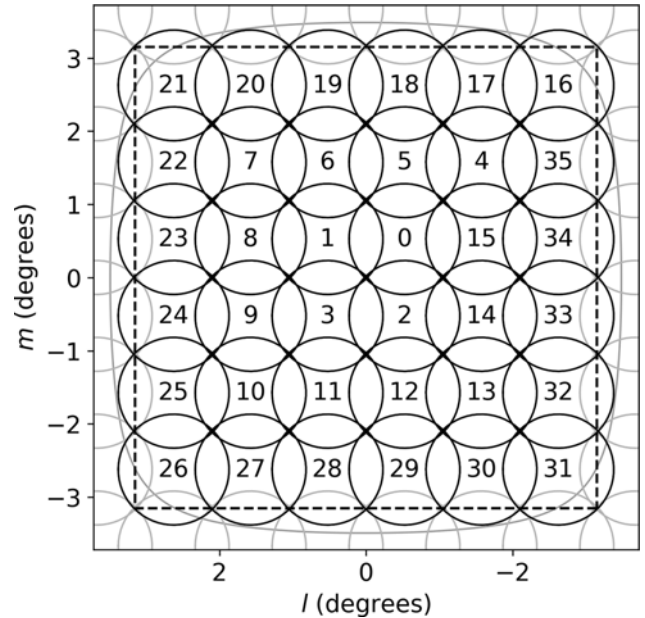

Figure 2. ASKAP field of view (l, m) using the `square_6×6` beam footprint. The positions of the 36 beams (numbered 0–35) are shown as idealised circles at their contour of half-power at 1031 MHz. In practice, the total intensity beams are close to circular at field centre but become increasingly elliptical towards the edge of the field with typical eccentricity of $e \lesssim 0.4$. The PAF sensitivity is greatest at the field centre, varies slowly over most of the field, and declines steeply at the edges; the outer grey contour shows the estimated locus of 50% sensitivity. Beams of adjacent non-overlapping tiles are also shown in grey.

PAF elements), so there is benefit to maximising beam spacing. Survey speed increases with beam spacing until the outer beams encounter the sensitivity drop at the edge of the field of view. On the other hand, minimal sensitivity ripple across the tile and freedom from polarisation leakage far from beam centres is achieved by decreasing the beam spacing.

Images are produced for each tile as the linear mosaic of the images made from each beam. Each beam image is made over an area that, for most of the frequency range, covers the main lobe of that beam; that is out to or beyond the beam pattern's first null. This provides significant overlap between beam images.

ASKAP uses two geometries in its beam footprints: square and hexagonal.[d] The square footprint provides a better match to the shape of the field of view, whereas the hexagonal pattern has lower sensitivity ripple and polarimetric aberration. For the first epoch of RACS observations, beams were arranged in a 6 × 6 square grid with a 1.05 deg centre-to-centre separation (pitch) as shown in Figure 2. At the highest frequency in the band (1031.5 MHz), the maximum beam spacing (along the grid diagonal) is equal to the beam full width at half maximum (FWHM). See Section 3.3.2 for estimates of true beam shapes across this footprint.

2.3. Sky coverage

To sample the sky with uniform sensitivity, we construct a tiling of the celestial sphere with square tiles sized to match the beam footprint. Adjacent non-overlapping tiles are placed, so that beam separation across tile boundaries is unchanged. Figure 2 shows beams of adjacent tiles for the non-overlapping case.

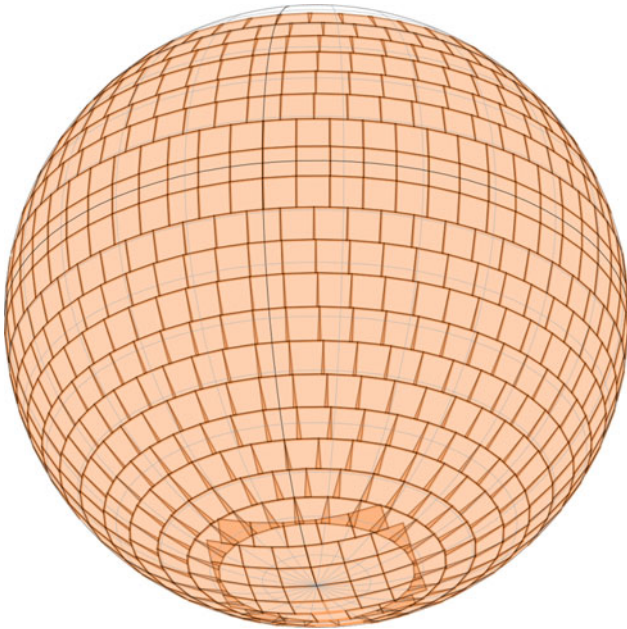[d]These are referred to as `square_6×6` and `closepack36`.

Figure 3. An orthographic view of the celestial sphere showing the arrangement of the RACS observing tiles. Ranks of tiles are centred on a series of declinations from +37.6 to –68.7°, giving full sensitivity from –71.3 to +40.2°. A quasi-rectangular grid of tiles is placed over the zone south of declination –71°, centred on the south celestial pole.

Tiles are arranged in rows along lines of constant declination; the number of tiles in each row is the minimum needed to span 360° of right ascension without gaps; successive rows are spaced in declination using the same criterion of no gaps but minimal overlap. Within about 20° of the pole, this pattern is replaced by a quasi-rectangular grid of tiles centred on the pole. Figure 3 illustrates this scheme.

The absolute northern limit of telescope pointing, $\delta = +48°$, is set by the observatory's latitude (26.7° South) and the 15° mechanical elevation limit of the ASKAP antennas. ASKAP is sensitive to the sky up to 3° from its pointing direction, and so RACS will cover the sky from the south celestial pole to a declination of $\delta = +51°$ (although the data presented here are south of $\delta = +41°$).

Overlap between tiles is unavoidable and varies with declination. Averaged over the sphere, about 6% of the surveyed area appears within the full-sensitivity bounds of more than one tile. This fraction is only mildly dependent on tile size (within the range useful with ASKAP) and on the chosen boundaries of the polar cap. As mentioned above, even for minimal overlap between tiles, the beam spacing is nowhere greater than it is within each tile, so that image sensitivity is maintained over tile boundaries. In regions of overlap, the sensitivity is improved.

Many sources will be detected in more than one tile, and many more will be detected in several beams. These multiple detections will be used in the analysis of beam and tile-specific systematic errors, and the tile–tile overlaps will give some visibility of variability on the radio sky.

2.4. Sampling the angular-scale spectrum

The ASKAP antenna configuration was designed to maximise the sensitivity for extragalactic HI surveys (Gupta et al. 2008), but with additional elements added to the array centre and periphery to improve both the surface brightness sensitivity and resolution. The resulting configuration gives a good sensitivity on scales
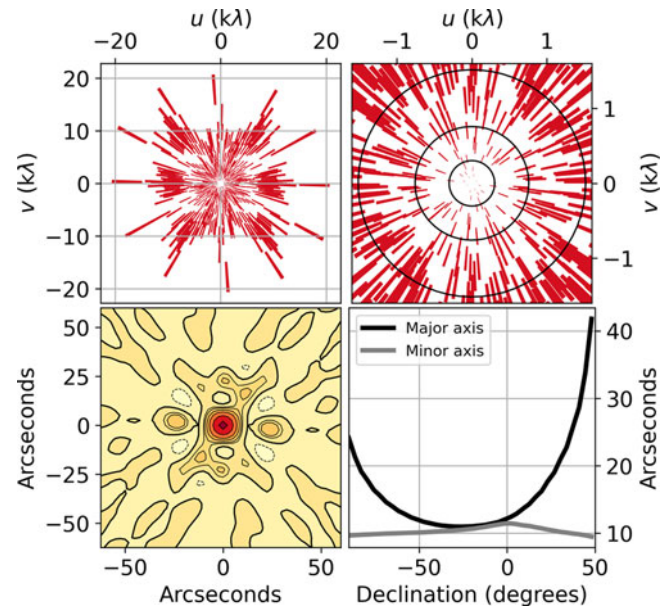

Figure 4. Sampling of (u, v) coordinates over a 15-min integration for a source near the zenith and the resultant point spread function (computed for the observing frequency of the first RACS observations). Upper left: whole (u, v) plane sampled. Upper right: inner part, showing that for extended structures the (u, v) sampling becomes sparse. The circles correspond to spatial scales of approximately 2 (outer), and 4 and 10 (inner) arcmin for observations made at 887 MHz. Lower left: the PSF; the contours lie at 0, ± 10, 15, 24, 37, 60, and 90% of the peak. Lower right: as a function of declination, the major and minor axis lengths of the main lobe of the PSF using this (u, v) sampling for observations made on the meridian.

from 10 arcsec to 3 arcmin (at 1.4 GHz, and with suitable visibility weighting). The distribution of samples of the (u, v) plane enabled by ASKAP's configuration is shown in Figure 4, scaled appropriately for this first set of RACS observations.

Without the benefit of Earth rotation, the inner part of the (u, v) plane is poorly sampled, making it harder to image larger angular scales with the short integrations used by RACS. The upper right panel of Figure 4 illustrates this limitation, which is most acute for spatial scales larger than 10 arcmin at 887.5 MHz (baselines shorter than 100 m).

2.5. The point spread function

The point spread function (PSF) depends on the distribution of projected baseline vectors and on the weighting scheme used for image formation. For the short integrations ($\sim$1000 s) used for RACS, the best resolution and PSF symmetry is obtained by observing on the meridian. Figure 4 (right, lower) shows the PSF major and minor axes (full major and minor axes of an ellipse at the half-height of the PSF) as a function of field declination, assuming a weighting scheme parameterised by robustness $r = 0.0$ ($-2 < r < 2$: Briggs 1995).

The RACS tile images are composed from 36 beam images, each having different sampling of the (u, v) plane, and so different PSFs. Even for the ideal case of an observation on the meridian with no data flagging so that all beams use the same set of antennas, the variation in PSF size over the field of view exceeds 15% at extreme northern and southern declinations (see Figure 4—lower right). This variation increases for observations away from the meridian and in the realistic case of data from some antennas being unusable for some beams.

2.6. Polarimetry

A detailed description of the RACS polarisation performance and calibration will be presented elsewhere (Thomson et al. in preparation). In summary, RACS beams are formed in paired (i.e., co-located on the sky) linear X and Y polarisation, with zero relative phase by construction (Chippendale & Anderson 2019). ASKAP's roll axis is driven to maintain the position and orientation of these beams and their planes of polarisation on the sky, simplifying polarimetric calibration and imaging (described further in Section 2.7). Thus, Stokes I, Q, U, and V can be reconstructed for each 1-MHz frequency channel in each beam.

2.7. Calibration

2.7.1. Beam forming

The RACS observations use the standard ASKAP calibration procedures. Each of the 36 beams are formed with weights that maximise the signal-to-noise ratio in the direction of a strong point source; the Sun is used (Hotan et al. submitted). These weights accommodate the different gains of the PAF elements. Each antenna has an ODC—an 'on-dish-calibrator' system that radiates a signal from the vertex of the primary reflector and records the response from each PAF element (Chippendale & Anderson 2019). This is used to track changes in PAF element gain and allows beam weights to be adjusted in compensation. Also, the ODC provides a polarised reference signal that is used to align the phase of each dual-polarised beam, that is to set the so-called 'XY–phase' to zero.

2.7.2. Antenna gains

The primary calibration of the various aspects of antenna gain is done with an observation of PKS B1934–638, the primary cosmic reference source for ASKAP. The term 'antenna gain' normally refers to those aspects of the synthesis telescope's response that can be factored into antenna-specific quantities. For ASKAP, we use that term for each beam formed on an antenna. With its 36 formed beams, ASKAP is effectively 36 parallel synthesis telescopes for which each beam is the equivalent of an antenna in a conventional telescope.

For each science observation, ASKAP observes PKS B1934–638 with each beam in turn. The pointing direction and roll axis of the antennas are adjusted, so that the reference source lies in the target beam centre and that the instrumental polarisation direction has the same relation to celestial coordinates for all beams. These data are used for:

Band-pass calibration and flux density scale: The known spectral energy distribution of PKS B1934–638 (Reynolds 1994) is used to calibrate both the instrumental band-pass shape and the absolute flux density scale (but see Section 3.4.4 below for more details).

Interferometer phase: ASKAP maintains a separate phase and delay tracking reference position in the centre of each beam. Antenna gains are set so that visibility phases on all baselines are zero in the PKS B1934–638 data, fixing the position reference for images of the science field. Astrometric accuracy in the science field images may be limited by electronic drifts in the signal path and by differences in path through the atmosphere between the calibration and the science observations.

On-axis polarisation leakage: At decimetre wavelengths, PKS B1934–638 is less than 0.1% polarised (Schnitzeler et al. 2011)

Table 2. First epoch observation parameters.

Frequency	887.5 MHz
Bandwidth	288 MHz
Sky coverage	$-90° < \delta < +41°$
Tiling	903 tiles (see Figure 3)
Integration per tile	15 min
Footprint	`square_6×6`
Beam spacing	1.05°
Surveyed area	34 240 deg^2

and the polarised emission from nearby sources is negligible. Any observed polarisation therefore arises from coupling between the X and Y beams and is used to determine coefficients in the feed-error matrix **D** (Hamaker & Bregman 1996), the so-called leakage 'D-terms'. For ASKAP, these are found to be low and stable and dominated by a real-valued offset (corresponding to non-orthogonality for the X and Y dipoles) with a magnitude of up to 1%, but typically less than 0.5% (Sault 2014; Anderson et al. 2018).

2.7.3. Wide field instrumental polarisation

ASKAP's formed beams are similar across antennas and maintain their position and orientation on the sky (Section 2.6). Thus, the pattern of instrumental polarisation over each beam should be stable, and so amenable to being characterised, leading to an image-based correction. Sault (2015) has described such a process but points out that it will be complicated by any significant time variation of ionospheric Faraday Rotation. The development of a wide field polarisation calibration procedure is required before the release of RACS polarisation products.

3. Early survey results

3.1. Observations

In this paper, we present results from the first complete epoch of RACS. The first all-sky observations began on 2019 April 21 using the parameters given in Table 2. Observations were scheduled automatically, sequencing each field optimally given a number of constraints that included elevation and distance from solar system bodies. The optimisation took account of the relative availability of fields, mainly determined by time above the horizon, and time-consuming telescope operations such as the rotation of the roll axis.

Initial sessions in April and May omitted the region around the south celestial pole and fields within about 5 degrees of the Sun. The southern tiles were observed in 2019 August, and tiles originally omitted around the Sun, and some others affected by the Moon or instrumental failure were observed from 2019 October to November. As mentioned in Section 3.4.2, many of the early observations were made at a large angular distance from the meridian. The scheduler was improved by adding an hour angle constraint and the most affected fields were then re-observed from 2020 March to June. Table 3 lists the dates of all the observations.

PKS B1934−638 was observed for 200 s with each beam, typically once per day. Data from these observations were used for calibration as described in Section 2.7.2. Experience with ASKAP has shown that antenna gains are stable enough to allow calibration of science data up to about 24 h after the calibration is taken. Short-term (minute-scale) gain fluctuations are small and can be

Table 3. First epoch observation dates.

Dates	Fields
2019	
April 21, 22, 24–30	692
May 4, 6, 7	177
August 3, 17	31
October 31	13
November 8	8
2020	
March 26–29	123
April 30–May 4	168
June 19–21	24

corrected with self-calibration as described in Section 3.2. Longer-term gain amplitude variations are quantified as part of the flux density calibration described in Section 3.3.

3.2. Calibration and imaging

RACS data were processed by the ASKAPSOFT package (Cornwell et al. 2011a; Guzman et al. 2019) using the *Galaxy* computer cluster that is maintained at the Pawsey Supercomputing Centre. The software is organised into a pipeline—the sequence of ASKAPSOFT applications used to select, flag, calibrate, and image the data. The pipeline software accepted parameters for controlling how each step is conducted, and the whole system is organised so that all RACS fields were processed consistently.

The following steps were taken:

Selection: visibility data from both the calibrator and science fields were copied from the raw MeasurementSets;

Flagging: anomalous samples in the data from both calibrator and science fields were identified using both fixed and dynamically set thresholds in amplitude and excluded from further use; data judged to be poor following calibration steps were also excluded;

Primary calibration: data from the observations of PKS B1934−638 were used to determine the frequency-dependent gains for each beam as described in Section 2.7.2, establishing the instrumental flux density scale and interferometer phase for each beam centre, as well as factors to correct the on-axis polarisation leakage.

Imaging (total intensity): calibrated multi-frequency visibility data for each beam were gridded and imaged as the first two terms (0, 1) of a Taylor series using multi-frequency synthesis. Self-calibration was performed: each beam image yielded a field model that was used to derive a set of antenna gain adjustments. For RACS data, this cycle was run twice; that is each beam was imaged three times, the second and third after a gain adjustment derived from the previous image. (In future, the sky model derived from RACS may be used in this process.)

Images for each beam were made with 6144×6144 cells of size 2.5 arcsec. This is the largest image size practical using the *Galaxy* computer cluster in its current configuration. Each beam image has a $4.2°$ extent, which covers the main lobe of the primary beam at the high-frequency end of the band and reaches the 4% sensitivity level at the low-frequency end (see Figure 5). The weighting of visibility measurements is achieved by *preconditioning* (Rau
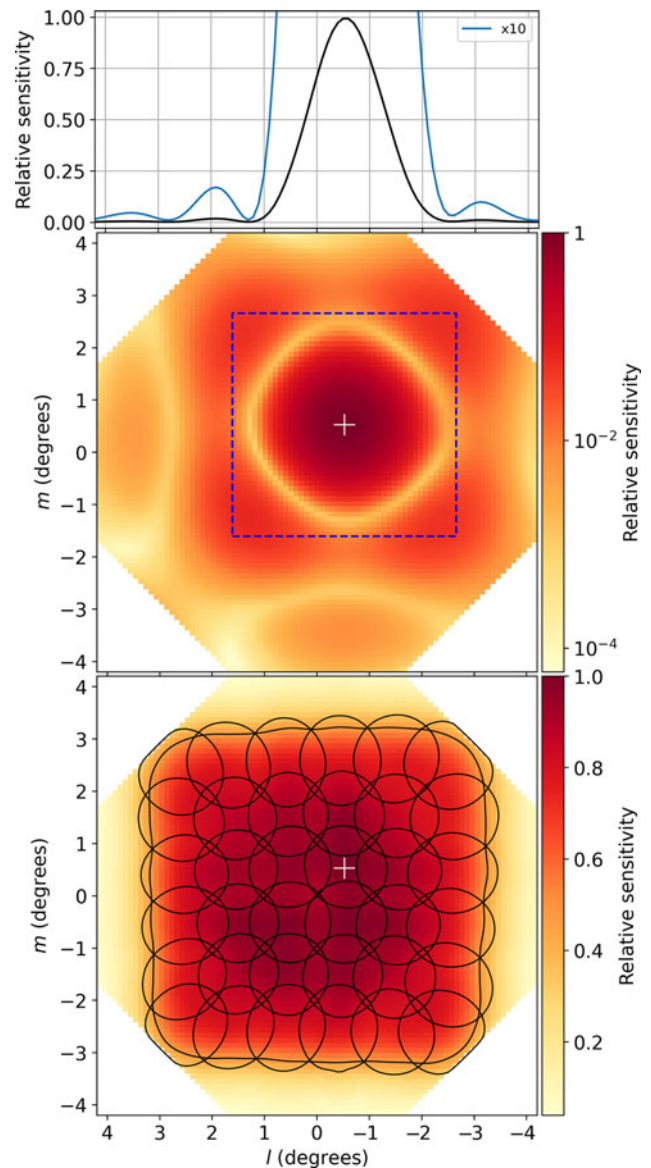

Figure 5. Primary beam sensitivity patterns determined by holography. The central panel shows, on a logarithmic scale, the sensitivity pattern for beam-0 at 930 MHz, which in the RACS footprint is offset $0.525°$ from the field centre in both cardinal directions. This display clearly shows the corner regions of the field not sampled during the holography measurements. The dashed square marks the boundary of the image made for beam-0. The top panel shows the variation of sensitivity on a linear scale, horizontally through the beam centre. The bottom panel shows all beams as contours at their half-power level. An estimate of the sensitivity of the 36-beam mosaic is indicated by the density of shading, with the outer contour drawn at the 50% level. The white cross in bottom and central panels marks the intended centre of beam-0.

2010), an approach designed to minimise data access load on the software. RACS imaging used preconditioning that achieved the equivalent of a Briggs (1995) 'robust weight' of $r = 0.0$ (r lies in [-2,2]). The Briggs weighting scheme provides a continuum between the extremes of 'natural' (gridded data weighted by the number of measured points) and 'uniform' (all gridded data given the same weight). The value $r = 0.0$ gives a compromise between sensitivity, maximised with natural weights, and resolution, better with uniform weights.

Deconvolution used the BASISFUNCTIONMFS algorithm,[e] which supports multi-scale cleaning. It was done in many 'minor cycles', in which an approximation of the PSF centred on the maximum residual at each iteration was subtracted from the image, and fewer 'major cycles' in which the modelled sources were subtracted from the visibility data. For the RACS imaging, major cycles used a W-projection algorithm (Cornwell, Golap, & Bhatnagar 2008) to correct for the effects of non-coplanar baselines with 512 W planes out to a maximum of 26 000 wavelengths. Each major cycle used a target peak residual of 1 mJy beam^{-1}. The minor cycles used residual thresholds that decreased with each self-calibration cycle: 100, 10, and 1 mJy beam^{-1}. In the final imaging cycle, we used three cleaning scales of 0, 20, and 50 pixels.

Full complex gain corrections (amplitude and phase) were determined in the self-calibration step, but the solutions were normalised before use to approximate the traditional 'phase-only' self-calibration. Visibility data from short baselines (<200 m, corresponding to angular scales greater than 5 arcmin) were not included in the self-calibration gain determination, preventing corruption from poorly modelled extended sources in the image.

Many fields close to the Galactic Plane were difficult to image because of nearby bright and extended emission; the short RACS observations have limited capacity to represent these well (see Section 2.4). Of the 146 fields within 10 degrees of the Galactic Plane, 67 were imaged without visibility data from baselines shorter than 35 m. Solar emission also caused similar difficulties for some fields: 63 fields were imaged with baselines shorter than 100 m excluded. The minimum baseline length used for each RACS image is recorded and released in the survey database (see Section 4).

Calibration application: gain adjustments from the self-calibration and from polarisation leakage calibration were applied to the visibility data, which can then used for any further imaging.

Mosaicing: all beam images were combined into a single image for the whole tile; at each point, the final image is a linear combination of the overlapping beam images using the primary beam model described below.

3.3. Flux density calibration

The ASKAP intensity scale is tied to the flux density of PKS B1934–638 whose spectral energy distribution is described by Reynolds (1994); the scale is set independently for each beam with an observation of that source. ASKAP images are mosaics of the 36 beam images. Over the course of the RACS observations, we have had incomplete knowledge of the beam reception patterns and the efficacy of the flux density calibration. Although the mosaicing operation assumes regular and identical beam shapes, we know that to be an approximation. The disposition of calibration and science observations varies with respect to their relative times and elevations in the sky; the precise effect of these variations on the flux density calibration is unknown.

In the light of these, we seek to quantify the flux density scale as functions of position (l, m) in the footprint and of observation time t. We compare total flux densities S_{RACS} of sources in each RACS image with that of their counterparts in either or both of the SUMSS and NVSS catalogues. We form ratios $R_x = S_{RACS}/S_x$

where $x \in$ [SUMSS, NVSS] and suppose that

$$R_x = \left(\frac{f_{RACS}}{f_x}\right)^{\alpha_x} F(l, m, t), \qquad (2)$$

where f is the radio-frequency of the survey, α_x is the characteristic source spectral index between the two survey frequencies, and F describes the unknown variations in flux density scale. We make the simplifying assumption that

$$F(l, m, t) \simeq F_1(l, m)F_2(t) \qquad (3)$$

is the product of two independent functions. Cast in this way, estimations of functions F_1 and F_2 can be made without knowing the values of α_x, provided we retain reliance on the absolute scale determined from PKS B1934–638. Specifically, we assume that averaged over time, the flux density scale derived from the calibration data is accurate and free from systematic error.

Until recently, measurements of the beam pattern have been insufficiently repeatable to assume anything but a simple average shape for all beams: a circular gaussian with width at half-power of FWHM $= 1.09\lambda/D$, where D is the antenna diameter and λ is the wavelength of the observed radiation. All ASKAP images, including RACS images, have been produced by linearly mosaicing beam images using that assumed pattern.

Analysis of source flux densities in RACS images has revealed inconsistencies: (i) in comparison to other standards, flux densities measured in RACS images were ∼10% too high and (ii) there were clear indications that this discrepancy was not uniform, but dependent on source position within a tile. We were led to review the standard mosaicing procedure and the transfer of flux density scale from the primary calibrator, as described below.

3.3.1. Flux density comparisons

Comparison of RACS source flux densities with values recorded in the SUMSS and NVSS catalogues has followed a procedure designed to make an unbiased estimate of the RACS flux scale anomaly. To avoid the complexity of accounting for the variable PSF (see Section 2.5), a large subset of RACS images were convolved with a gaussian function to give each a uniform (and circular) PSF with width 25 arcsec. The image analysis tool SELAVY (Whiting & Humphreys 2012), which uses the Duchamp source finding algorithms (Whiting 2012), was used (with its default parameters) to identify sources in these images. Comparison sources were chosen to have a nearest-neighbour separation $\Delta\theta_N > 90$ arcsec, a separation from SUMSS or NVSS counterpart of $\Delta\theta_m < 10$ arcsec, and a signal-to-noise ratio SNR $= S_p/\sigma \geq 10$, where S_p was the peak flux density and σ the root-mean-square (rms) image noise at the source location. To ensure that chosen sources were unresolved, we used the following procedure (see also paper II). For all single component sources within a Selavy catalogue, we examined the total to peak flux density ratios $r_S = S_t/S_p$. For unresolved sources, the distribution of this quantity should have unit mean and variance proportional to SNR^{-2}. Resolved sources appear as positive outliers. We determine the 5th percentile as a function of SNR to define a lower envelope to the distribution (Bondi et al. 2008; Smolčić et al. 2017), which we describe as $r_{S_L} = 1 - A \times$ SNR^{-B} where A and B give the best fit. This allows an estimate of the distribution's upper envelope, which is obscured by the presence of resolved sources, to be estimated as $r_{S_U} = 1 + A \times$ SNR^{-B}. All sources with $r_{S_L} < r_S < r_{S_U}$ were defined as unresolved, which led to a total of 67 595 sources identified for the following analysis.

3.3.2. Position-dependent variations

To quantify the direction-dependent variation of flux density scale, comparison ratios (S_{RACS}/S_{SUMSS} and S_{RACS}/S_{NVSS}) of the source sample were binned according to the source positions (l, m) relative to the optical axis, and the median determined for each bin. Only the relative fluctuations over the field of view were needed, so both sets of ratios were scaled to have mean 1.0. The result is an estimate of $F_1(l, m)$ in Equation (3) and is shown in the left panel of Figure 6. It shows a fourfold symmetry across the field, suggestive of incorrect primary beam correction.

Beam shape measurements Beam patterns for the RACS footprint were measured on 2020 February 6 using holography and the procedure described by Hotan (2016). The new measurements were significantly more consistent than earlier attempts, showing less antenna to antenna variation in beam shape. We attribute this improvement to the advances made over the past year in phased array set-up and calibration. The measurements yield complex voltage measurements as a function of frequency for each beam on each antenna (apart from a reference antenna) on a grid of points covering the field of view. For our application, a robust array-wide mean power pattern was constructed for each beam, resulting in 36 beam maps for each of the 288 frequency channels. Interpolation was used to span gaps in the spectrum caused by RFI. Figure 5 shows the mean pattern for beam-0 over 26 of the 32 measured antennas (the missing four were the reference antenna and three others that were unavailable during the holography observations) and the measured shape at half-power of all beams in the footprint. All of the 26 antennas used for the array-wide mean had power patterns differing from the mean by less than 4%. The antennas not used in the mean pattern were the outer six; the holography procedure uses the source Virgo A as a reference and because of its angular size, it has insufficient power on the longest ASKAP baselines to make reliable beam measurements on those outer antennas.

Flux density scale correction If B_m is the image brightness determined using the standard reception pattern assumption A_i for each beam, and H_i is the pattern as measured by holography, then

$$B_t = B_m \frac{\sum A_i^2}{\sum c_i H_i A_i} \tag{4}$$

is the true brightness. In Equation (4), c_i corrects for the effect of a coma-related asymmetry in beam shape moving the peak response away from each beam's nominal position. Ideally, without coma, $c_i = 1.0$. However, we measured values of $0.92 < c_i < 1.0$, the most extreme values for outer beams at the low-frequency end of the band. This was a major cause of the high flux densities measured in RACS images. Appendix A describes the derivation of Equation (4) and its use to correct both the zeroth and first Taylor term images.

Figure 6. (centre) shows the evaluation of the factor $C_0 = B_t/B_m$ in Equation (4). No holography measurements were made outside the heavy dashed lines in that Figure.

Note that this flux density comparison was constructed from observations made over many months, most of them several months before the holography measurements. The degree of similarity between the left and centre panels indicates a pleasing level of stability of ASKAP beam reception patterns. In future, holography beam measurements will be made routinely as part of

the instrumental flux calibration, and the values of H will be used directly by the linear mosaicing software so avoiding the use of Equation (4) and the procedure described here.

Although there is clear similarity between the forms of the measured and predicted intensity scale errors, the calculated factor B_t/B_m is insufficient for a full correction of the RACS image intensity scale. Both the incomplete holography measurements and the probable failure of the single measurement to represent actual beam reception patterns earlier in the survey contribute to this inadequacy. Therefore, we have used the same set of flux density ratios of the 67 795 source sample described above to determine a multiplicative adjustment C_1 to improve the correction in areas of the field poorly characterised by holography. Flux density ratios were again binned according to position (l, m); median values were determined for each bin and normalised to give a mean value of 1.0 over the area of valid holography measurements. The normalisation was done independently for the S_{RACS}/S_{SUMSS} and S_{RACS}/S_{NVSS} ratios, allowing the two surveys to be used in this way in spite of their different centre frequencies. By forming the flux density correction in this way—constraining the mean correction over the holography field and using the source sample drawn from most of the RACS survey area $-84° < \delta < +30°$, (SUMSS: $\delta < -30°$; NVSS: $-40° < \delta < +30°$), we have retained the link to the original flux scale calibration with PKS B1934−638. Thus, any change in the mean flux density measurements is a result of the improved primary beam models, not the comparison with SUMSS and NVSS. The factor $C_1(l, m)$ is shown in the right-hand panel of Figure 6. The correction applied to all RACS images was $F_1(l, m) = C_0 C_1$.

3.3.3. Time-dependent variations

With the large offset-dependent scale errors removed, we examined the data for evidence of other forms of systematic error. Such errors may be expected from a number of factors such as a dependence on the zenith angle of the observation, temporal and angular distance from the calibration observation and variation in receiver gains. Figure 7 shows the variations in apparent intensity scale against the observations' position in their time-ordered sequence. The separation between RACS/SUMSS and RACS/NVSS points in the top panel arises from the different survey frequencies and the typical negative spectral slope of radio sources. As with the position-dependent analysis above, we are interested in changes in the RACS flux density scale, not in its mean value and so the bottom panel shows the two series with the mean removed and is an estimate of $F_2(t)$, Equation (3). There is evidence of a non-random component in the variation: note the similarity in fluctuations between the two series in the observation sequence range [500,600].

As a trial, we have computed an extra scale factor for each observation from a smoothed form of this series. When this was applied to the images, there was no clear improvement: no decrease in the overall variance of flux scale and no significant change in the implied average spectral index between RACS sources and counterparts in catalogues formed at other frequencies. Therefore, and because we do not yet understand the physical origin of the non-random scale variation, we have not made any further correction to RACS image intensity scales.
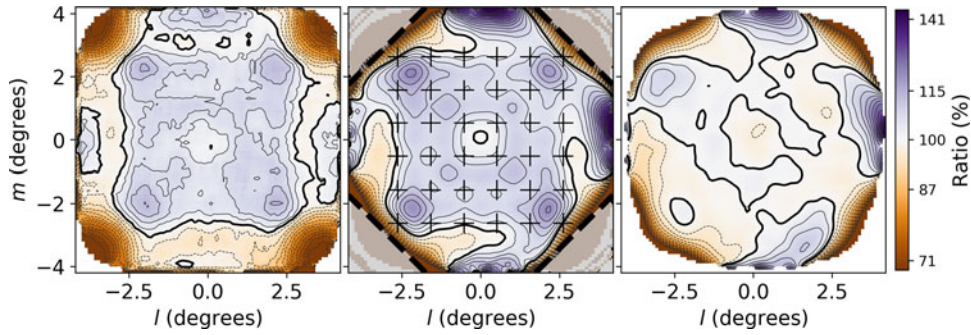
Figure 6. Brightness calibration over the field of view. Left: the flux density ratio of RACS sources (uncorrected) to their counterparts in the SUMSS and NVSS catalogues, determined as described in the text (Section 3.3). Centre: the direction-dependent correction C_0 derived from holography beam measurements and Equation (4); the corners of the field, outside the dashed lines, were not sampled by the holography procedure; beam positions are marked with a +. Right: the extra multiplicative factor C_1 used with the values in the centre panel to correct the flux density scale variations; it shows the extent to which the holography-based correction matched the flux density comparison data—very well across most of the field, and poorly near the edge of the holography grid. In all panels, the contour interval is constant in the logarithm such that adjacent contours differ by a factor of 1.03, with the heavy contour at 1.0.
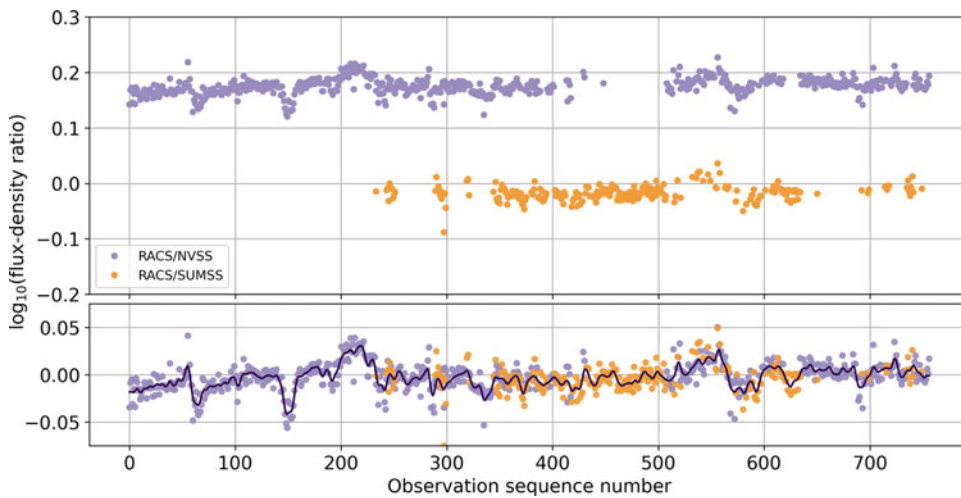
Figure 7. Apparent flux scale variations. The abscissa in both panels is the sequence number of each observation. The upper panel shows, for each tile, the median flux density ratio between RACS and NVSS and SUMSS measures as their logarithms. No allowance has been made for the different frequencies of the surveys; typical source spectral indices shift the two sets of points away from unity—$S_{RACS}/S_{SUMSS} < 1$ and $S_{RACS}/S_{NVSS} > 1$. The lower panel has both sets of ratio logarithms shown with their means subtracted. The ratio variations appear to have a random component added to a slowly varying component with typical scale of 10–20 observations and shown as a dark line.

3.4. Image quality

In this section, we present quality assessments for the first epoch RACS observations: image noise and sensitivity, astrometric precision and accuracy and photometry—the flux density scale. We also give some general comments on the image fidelity, the degree to which images are representative of the true sky brightness. We leave thorough analyses of survey completeness and reliability to the RACS paper II currently in preparation.

3.4.1. Image noise

For each image, we generated a noise map by dividing the image into cells of 100×100 pixels and in each, measuring the signal spread about the mode, allowing an estimation of the *rms* noise without contamination by compact sources in the image. Figure 8 shows some example noise images. These views of the survey products show clearly the variation of sensitivity across the field of view. They also show that for these observations, there is little sensitivity ripple imposed by the grid of beams within the tile.

The upper right panel of Figure 8 indicates the beam positions and width (at the centre frequency). The right panel also shows the variation of sensitivity across the tile boundaries.

Figure 8 also illustrates another feature of the images: increased noise close to bright sources. For example, the noise peak seen in the upper left of the left panel surrounds PKS J1102 –0951, a source with a flux density of 0.9 Jy in the RACS image.

Figure 9 shows the distribution of rms noise values for RACS Stokes I images. The median *rms* noise is $\sigma_{med} = 250\,\mu$Jy beam^{-1} and 90% of RACS images have $\sigma_{med} < 330\,\mu$Jy beam^{-1}. The median rms of all RACS images is shown in Figure 10.

3.4.2. Point spread function

As mentioned in Section 2.5, the variation in PSF size across a single tile mosaic can be significant because of large baseline foreshortening gradients across the field of view, and also beam-specific data losses due to instrumental problems. The latter became less acute through the observing period because of
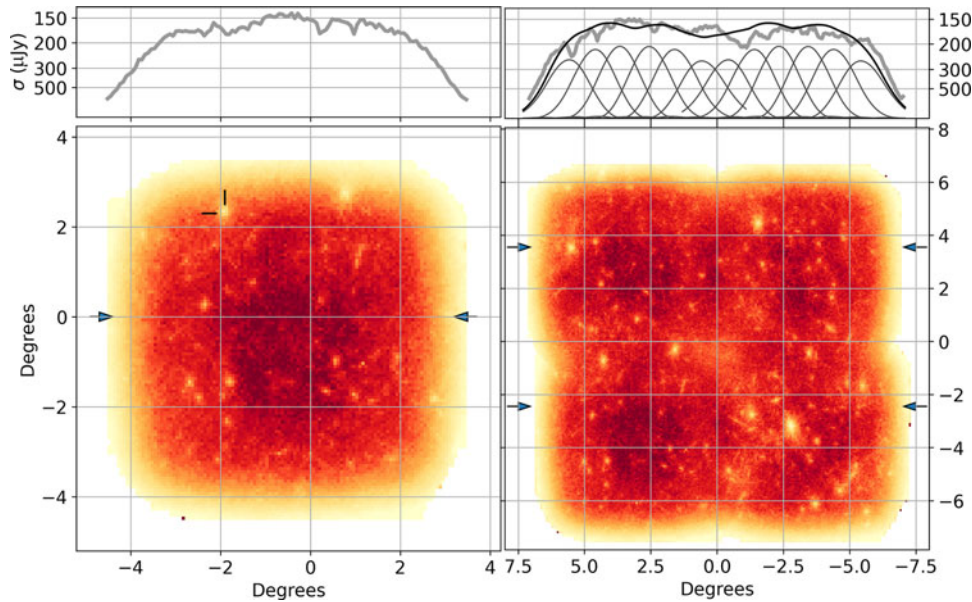
Figure 8. Image noise displayed as the inverse *rms* $(1/\sigma)$ computed as described in the text (Section 3.4.1). For each, the upper panel shows a horizontal profile (grey line) averaged over the range indicated by the arrows beside the images. Left: the variation of noise amplitude across a single Stokes-I image tile; the central value is $\sigma \simeq 150$ mJy beam^{-1}. This tile is colocated with the bottom left tile of the right-hand panel. The feature marked is associated with the source PKS J1102 –0951 as described in the text. Right: the variation of image *rms* over a mosaic of four tiles. These tiles are centred at 1033-06, 1057-06, 1031-12, and 1056-12. In the top right panel, we also show the beam profiles along a horizontal path through beam-0 (between the arrows). The beam profiles are taken from the holography measurements described in Section 3.3.2 and weighted by a system noise estimated for each beam from the flux density calibration data record of PKS B1934–638. The beams shown are numbered as 23, 8, 1, 0, 15, and 34. The smooth black curve is the resultant sensitivity expected from these beams.
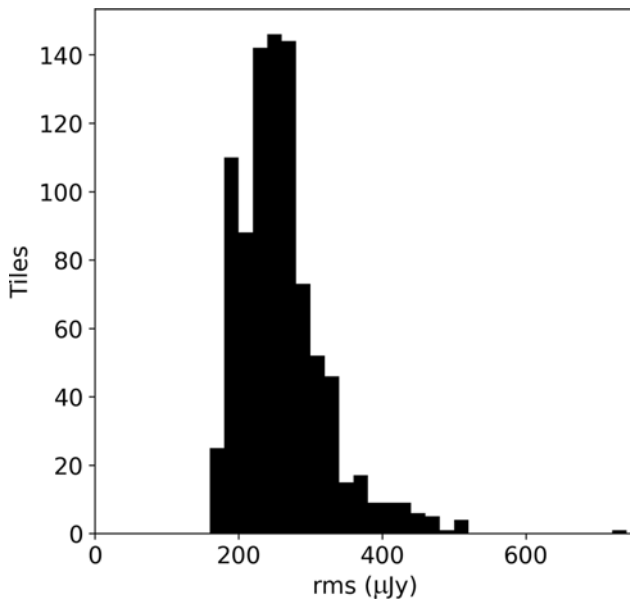

Figure 9. The distribution of the median *rms* values for the 903 tile images in the first RACS image release.

improvements in the telescope reliability. Although the differential foreshortening effect can be minimised by observing close to the meridian, some variation of PSF size and shape will always be a feature of ASKAP images.

We draw attention to the impact PSF size variation on photometric interpretations of the image. The intensity in an astronomical image is expressed in units of flux density per unit solid angle; in the case of radio images, the traditional measure is mJy beam^{-1}

where 'beam' stands for the solid angle Ω subtended by the main lobe of the PSF. In RACS images, $\Omega = \Omega(l, m)$ varies across the image so we must declare a reference PSF with solid angle Ω_{ref}. In practice, this reference is the PSF of the beam-0 image, and its parameters are recorded in the mosaiced image header. Then the total flux density S of a source at position (l, m) in the image I is

$$S = \frac{\Omega_{\text{ref}}}{\Omega(l, m)} \int_{\text{src}} Id\Omega. \qquad (5)$$

The expression is only applicable for computing the total flux density of a source; the brightness scale, including the peak flux density of sources, is correct without adjustment.

To support the use of the RACS image set, we release two forms of each image. First we provide the mosaic produced by the pipeline as described in Section 3.2. These images provide the highest, but variable, spatial resolution. With knowledge of the PSF variations over these images, source flux densities can be determined using Equation (5). Each beam image is restored using an analytic (elliptical gaussian) approximation of the main lobe of the PSF and then used to form the 36-beam mosaic. Therefore, at each point (l, m) in the mosiac, the effective or resultant PSF is the linear combination of the beam-specific gaussian functions, and we can approximate it with another elliptical gaussian whose volume is the PSF area $\Omega(l, m)$ in Equation (5) above. With each variable resolution RACS image, we publish its PSF area as a function of position in a separate file, enabling correct total flux densities to be determined by source finding software that uses the reference PSF information carried in the image file. Note that in some areas (e.g., around the celestial pole), the PSF of adjacent beams can differ markedly, making the effective PSF in the mosaic (the weighted mean of PSFs of overlapping beams) non-Gaussian and the results of source shape fitting less reliable.
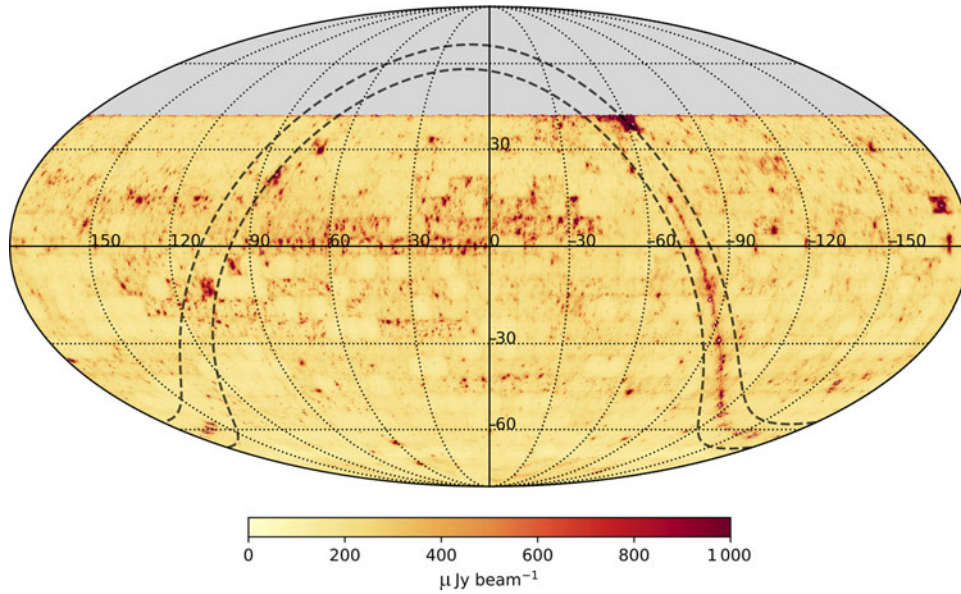
Figure 10. Image noise across RACS survey area derived from the 903 *rms* images described in Section 3.4.1. The Galactic Plane is visible over part of its longitude range. The prominent area with high noise near right ascension −170° and declination of 12° is the tile containing the source Virgo A, which is bright and has complex structure.

The second image type released is formed by mosaicing beam images that have been convolved to a common spatial resolution.[f] These images may lose some spatial resolution but can be used to estimate source flux densities without the need for Equation (5). For each RACS tile, using the methods provided by `radio-beam`,[g] we first find the smallest common PSF, that is, the PSF with the smallest area to which the set of 36 varying PSFs can be convolved. Second, for each beam i, we compute both the convolution kernel k_i required to transform PSF_i to that common resolution, and the scaling factor f_i required to maintain the image units of mJy beam^{-1}. We then produce common resolution beam image $I_{\mathrm{cmn},i}$ as the convolution of variable PSF image I_{var} with the convolving beam kernel:

$$I_{\mathrm{cmn},i} = f_i \left(k_i * I_{\mathrm{var},i} \right), \qquad (6)$$

for all beams in a tile ($i = 0, ..., 35$). These common resolution beams are then mosaiced as described above.

3.4.3. Astrometry

The astrometric performance of ASKAP (and all synthesis radiotelescopes) relies on the phase-tracking stability of the receivers and on the quality of phase reference measurements. ASKAP maintains a phase centre for each beam and so has 36 phase-tracking systems tied to the observatory frequency standard (a rubidium atomic clock; Hotan et al. submitted). RACS observations are referred to the phase observed during an observation of PKS B1934−638. In this section, we write astrometric errors as $\epsilon = (\Delta\alpha \cos\delta, \Delta\delta)$, a vector with components in the right ascension and declination directions.

Astrometric precision The overlap of ASKAP beams on the sky provides a means for assessing astrometric precision as there are typically 50 suitable sources that are common to any pair of adjacent beams. For each of these sources, we have two position

measurements and the distribution of their differences is observed to have both a random and a systematic component. Figure 11 (top) shows the position difference distribution for a single pair of adjacent beams in the field centred on $00^h00^m{-}37°38'$. The scatter in position is consistent with the expected position variance of

$$\sigma(\epsilon)^2 \simeq \Delta\theta^2 \times 2/(4 \ln 2 \times \mathrm{SNR}^2)$$

(Condon 1997); $\Delta\theta$ is the angular size of the PSF, SNR is the signal-to-noise ratio of the source, and the factor of 2 arises from differencing samples from two independent distributions. In this case, the PSF size is 16×13 arcsec and comparison sources have SNR > 20. The expected error ellipse is drawn in the figure, centred on the mean position.

The difference distribution has a non-zero mean: there is a systematic shift in apparent position difference of sources depending on which pair of adjacent beams is considered. The lower panel of Figure 11 shows the distribution of systematic shifts over all independent beam pairs for a sample of 567 RACS fields. Almost all shifts are less than the image pixel size of 2.5 arcsec. We attribute this systematic error to the effect of self-calibration, which is used for each beam image to improve the estimate of antenna gains. The improvement in relative antenna gain phases is achieved at the expense of introducing some uncertainty in absolute phase, resulting in small astrometric shifts.

Astrometric accuracy We have assessed RACS astrometry against the International Celestial Reference Frame (ICRF). The third realisation of the ICRF (ICRF3, Charlot et al. A&A, accepted) is a catalogue of 4 536 radio sources distributed across the sky; 3 604 of these lie south of the northern limit of RACS. At least one reference source appears in 506 RACS tiles. We matched ICRF and RACS sources, excluding matches for which the RACS source appeared resolved. The resulting 2 915 position differences $\epsilon = s_R - s_{\mathrm{ICRF}}$ are plotted in Figure 12, where s_R and s_{ICRF} are the directions to the RACS and ICRF sources, respectively. The east–west and north–south components of ϵ are distributed with means and standard deviations $\Delta\alpha \cos\delta = -0.6 \pm 0.6$ and $\Delta\delta = -0.4 \pm 0.7$

---

[f]Using https://github.com/alecthomson/RACS-tools.
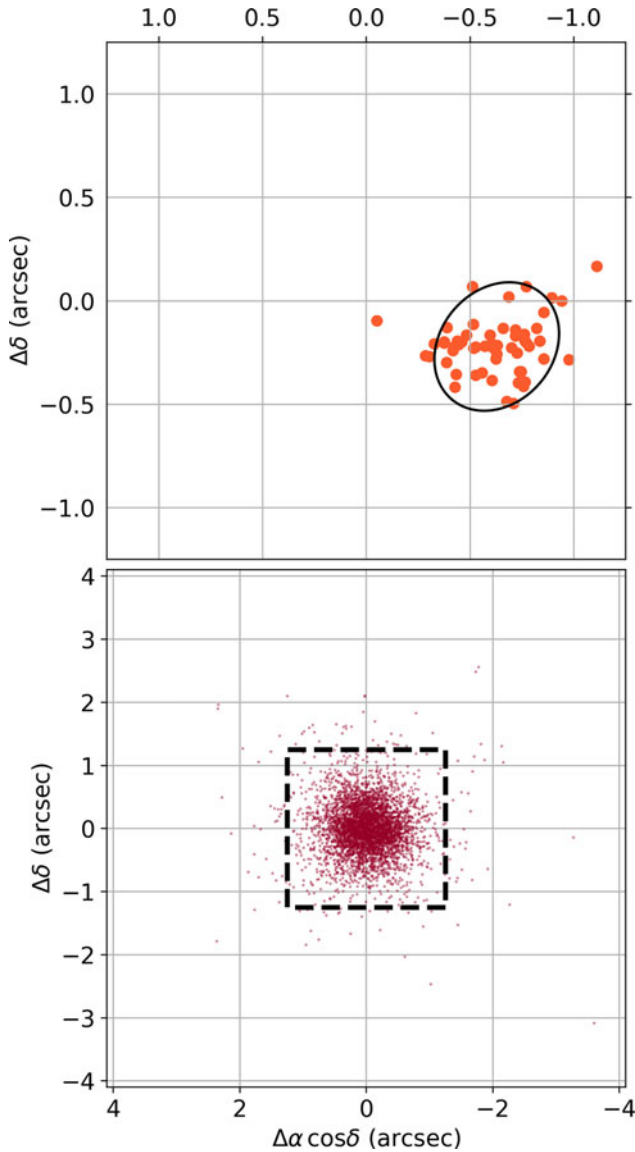[g]https://github.com/radio-astro-tools/radio-beam.

Figure 11. Beam-to-beam offsets. Upper: the apparent position differences of 57 sources observed in both beams 2 and 14 for the field centred on 00^{h}00^m –37°38′. The sources were selected to be compact and exceed a signal-to-noise ratio of 20, their spread consistent with expected error ellipse drawn in black. The upper panel is the size of each image pixel (2.5 × 2.5 arcsec). Lower: the distribution of mean beam-to-beam offsets over 16 beam pairs in 567 RACS fields. In most cases, the beam-to-beam astrometric difference is less than the width of a 2.5 arcsec pixel (dashed box).

arcsec. The error ellipse expected from Gaussian fitting considerations (Condon 1997) is shown in the figure, centred on the distribution mean and sized according to the survey-wide mean PSF shape (14.9 × 13.7 arcsec, position angle 53°) and SNR ≥ 10, with an additional component determined empirically from Figure 11. The cause of neither the mean position error nor its large variance is yet understood and will be the subject of future investigation.

3.4.4. Photometry

In Section 3.3, we discussed in detail the procedures that we devised to quantify and correct the intensity scale in RACS images.
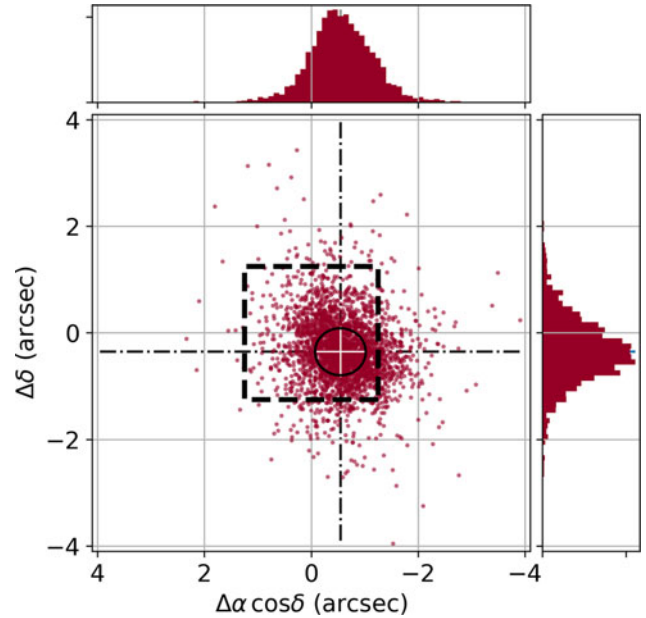

Figure 12. Position offsets of RACS sources relative to their ICRF counterpart. A systematic difference is observed; the median offset is –0.6 and –0.4 arcsec in right ascension and declination, respectively. The sources were selected to be compact and exceed a signal-to-noise ratio of 10. The text in Section 3.4.3 describes the basis for the size of the error ellipse drawn on the figure. The size of RACS image pixels is shown by the dashed square.

Figures 13 and 14 summarise the photometry over the survey images being released. The sky-wide comparison with SUMSS and NVSS catalogues is summarised in Figure 13, in which only the fluctuations about the mean flux density ratios are shown, the same fluctuations shown in the top panel of Figure 7. The non-random component to the position-dependent variation, in part, is associated to the Galactic Plane (the SUMSS catalogue excludes sources within 10° of the Plane). Other variations have unknown origin but likely correspond to the variations discussed in Section 3.3 and illustrated in Figure 7.

To quantify the uncertainty of source flux density ΔS in RACS images, we have analysed the values obtained for the set of sources that lie in the overlap between tiles and so have two independent measurements, each of which we assume to have the same uncertainty. For each source i, let the two flux density measurements be ^aS_i and ^bS_i, with mean S_i. We analysed the distribution of their ratios $r_i = {}^aS_i/{}^bS_i$, determining the standard deviation of r_i for a number of logarithmically spaced intervals in S_i. We found that the results were well modelled by the expression $\Delta S_i = \Delta S_0 + f S_i$ in which ΔS_0 and f are constants across the survey: $\Delta S_0 = 0.5$ mJy and $f = 0.05$. We add to this a component of uncertainty to reflect the variations seen in Figure 13, which we believe is independent of the errors evident in the dual-measure analysis. Adding in quadrature the standard deviation of fluctuations displayed in Figure 7, we arrive at a final expression:

$$\Delta S = 0.5 \text{ mJy} + 0.07S. \tag{7}$$

To check the absolute flux density scale, we examined the RACS flux densities of sources listed by Perley & Butler (2017), which have well-determined flux densities over the RACS spectral range. For each in the list, Perley & Butler (2017) indicate the extent of each source with a parameter LAS (Largest Angular Scale).
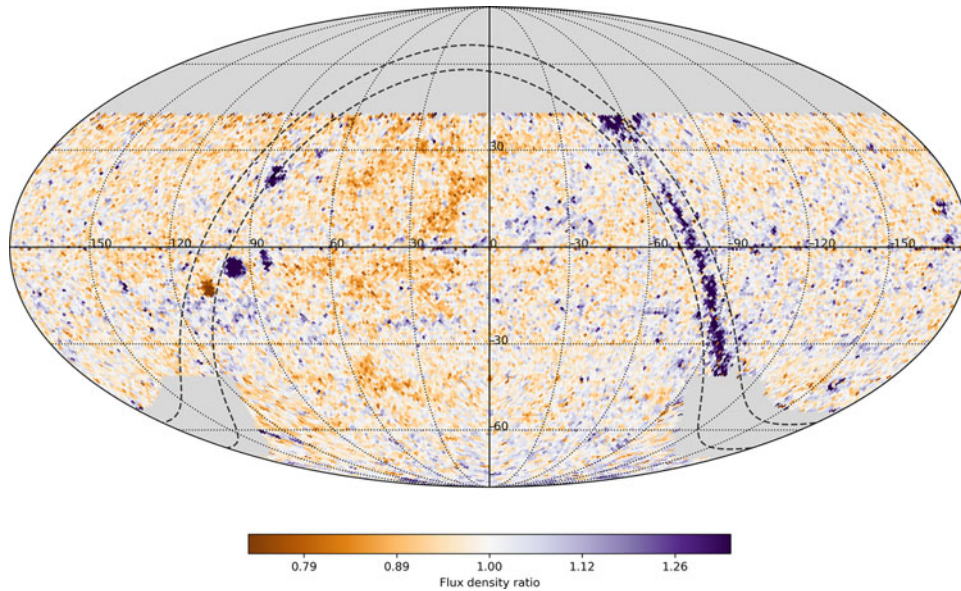
Figure 13. Apparent flux scale variations over the sky computed as described in the text. The Galactic Plane is visible as elevated values in the region covered by NVSS, and absent values over the SUMSS area. Galactic latitudes of $\pm 5°$ are shown.
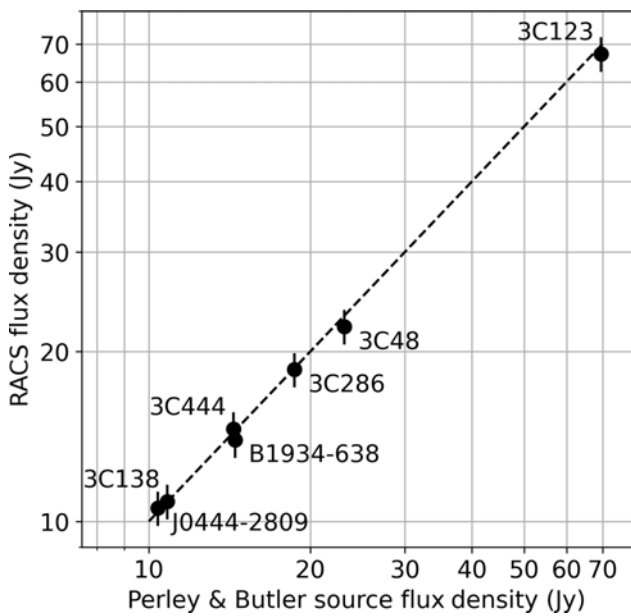

Figure 14. Comparisons of source flux densities measured in RACS images to those from a set of well-characterised sources published by Perley & Butler (2017) and Reynolds (1994). The error bars are computed from expression (7).

We have chosen the six sources south of $\delta = +40°$ with LAS $\leq$ 120 arcsec and added PKS B1934−638, also with well-determined spectral energy distribution (Reynolds 1994). Figure 14 shows the comparison; the error bar lengths were calculated from the expression (7). Several of the Perley and Butler sources are well resolved in RACS and their total flux density was found as the sum of component flux densities found by the Selavy image analysis tool. Note that the likelihood of all seven sources falling within one standard error of the expected value is very low ($\sim 0.68^{7} \simeq 0.07$), perhaps indicating that the value of f in expression (7) is too high.

3.4.5. Image fidelity

Radio images made with interferometers are typically able to well represent spatial scales from the size of their PSF up to a 'largest angular size' Θ_{LAS} determined by the length of the shortest baseline B_{min} as:

$$\Theta_{LAS} = \lambda/(aB_{min}),$$

where λ is the observing wavelength and a is a number $1 \lesssim a \lesssim 2$, depending on the observation length and amount of Earth rotation synthesis achieved. We make the distinction here between fidelity—the ability of the telescope to represent structures of a certain angular scale—and the telescope's sensitivity to those structures. Aperture synthesis telescopes necessarily have less sensitivity to larger scales because of the decreasing collecting area on short baselines. However, structures smaller than Θ_{LAS} can be imaged provided they are sufficiently bright. Source components with size greater than Θ_{LAS} are not sampled by the telescope and so cannot be imaged. For the brief RACS observations made at $\lambda \sim 34$ cm, we expect $25' < \Theta_{LAS} < 50'$. In regions close to the Galactic Plane, we had difficulty properly calibrating the shortest baselines and used only those longer than 35 m, so that in these images we expect $15' < \Theta_{LAS} < 30'$. Figures 15 and 16 show objects with a range of angular scales up to $\sim$15 arcmin.

Artefacts in the RACS images come in two varieties. The difficulty mentioned above with accurate use of the short baselines, in spite of excluding the very shortest, has led to broad artefacts positioned about bright extended sources, typically at a distance of 40–60 arcmin and having total flux density of 10–20% of the parent source. The second variety is an elevated variation in the background noise close to strong compact sources. The second term in expression (7) is in part a reflection of this, but around some very strong sources the problem is more severe. There is strong evidence that this variety of artefact is less common in more recently observed fields. Data collected earlier suffered from more system instability in beam band-pass shape.
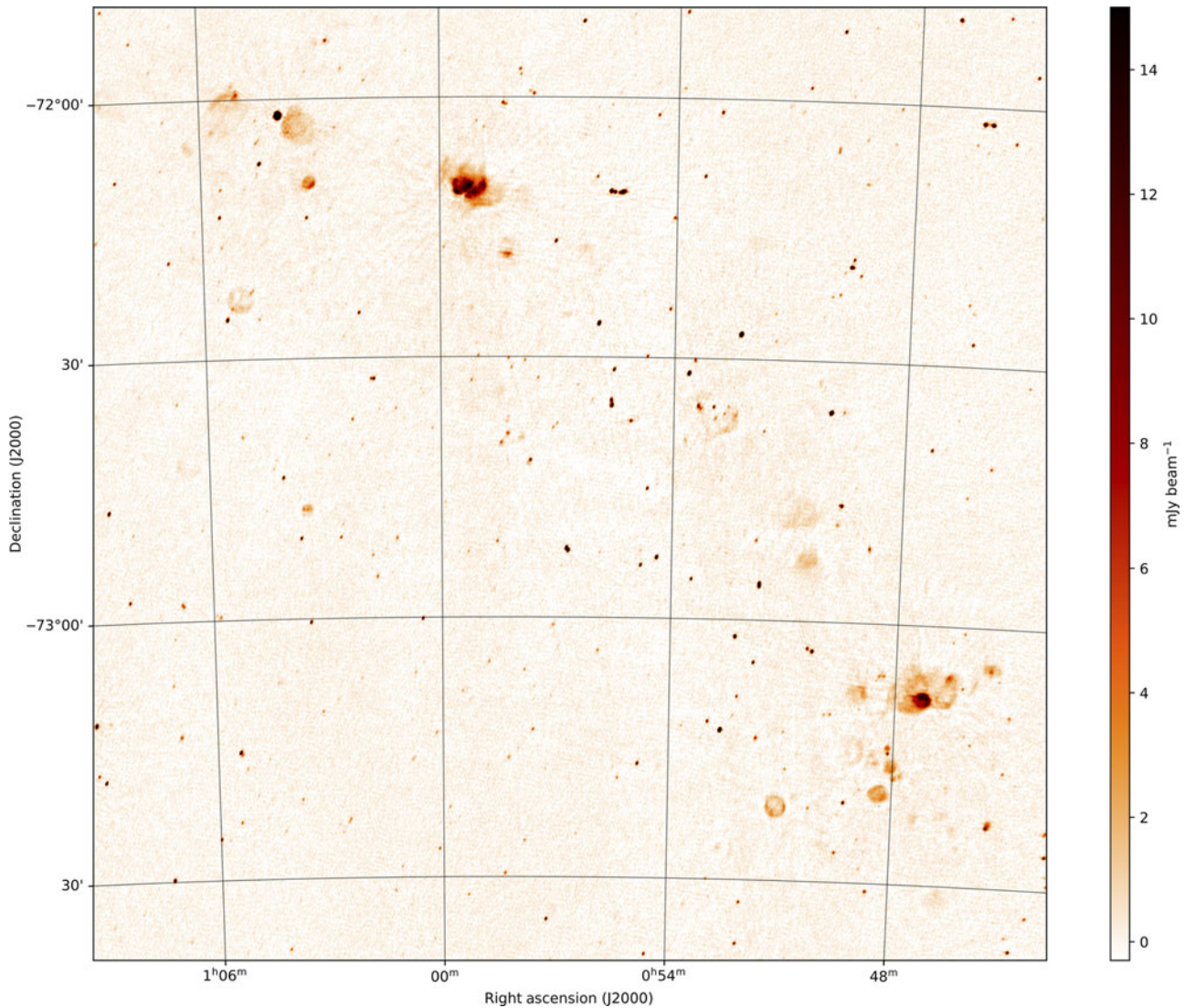
Figure 15. The RACS image of the Small Magellanic Cloud, as an example of a field with extended emission, with sources up to 5 arcmin in size being well represented. The *rms* brightness is $\sigma \sim 200\,\mu$Jy beam^{-1}. The PSF has dimensions 18.5×11.5 arcsec. The image has a dynamic range of about 3700:1. The bright nebula complex towards the top of the image is NGC 346 (also known as N66 and DEM 103), and to the lower right is N19 (DEM 32). A number of supernova remnant shells are visible, see, for example, Maggi et al. (2019) for details.

Figures 16 and 17 provide some comparison between images from RACS and other radio surveys. Figure 16 shows a portion of the Galactic Plane from the RACS and GLEAM surveys (Hurley-Walker et al. 2016). The GLEAM image has superior sensitivity to large angular scales, and the RACS image has the better resolution. Also evident is the differing spectral energy distribution of the objects in the field: thermal emission from HII regions is more prominent in the RACS image, while non-thermal emission from supernova remnants is brighter in the lower frequency GLEAM image.

Figure 17 shows a field imaged by all of NVSS, SUMSS, and RACS. The comparison shows clearly how better sensitivity and resolution of the RACS observations lead to more sources being detectable and to better definition in the extended objects.

3.4.6. Influence of solar system objects

Most of the first epoch of RACS observations were made within a 3-week period (2019 April–May) and so inevitably solar system objects appear in some images. Regions within about $6°$ of the Sun itself were avoided and observed at a later date. A number of tiles close to the Sun bear the effects of contamination by solar radiation on the short baselines, which were minimised by excluding data from baselines shorter than 100 m.

The Moon appears in two of the tiles, which were also re-observed later. Jupiter is visible close to the boundary of two tiles, observed on 2019 April 25 and 2019 April 27. It appears as an extended source of total flux density $\sim$3.8 Jy. Saturn and Mercury are also visible with flux densities of 20 and 4 mJy, respectively,
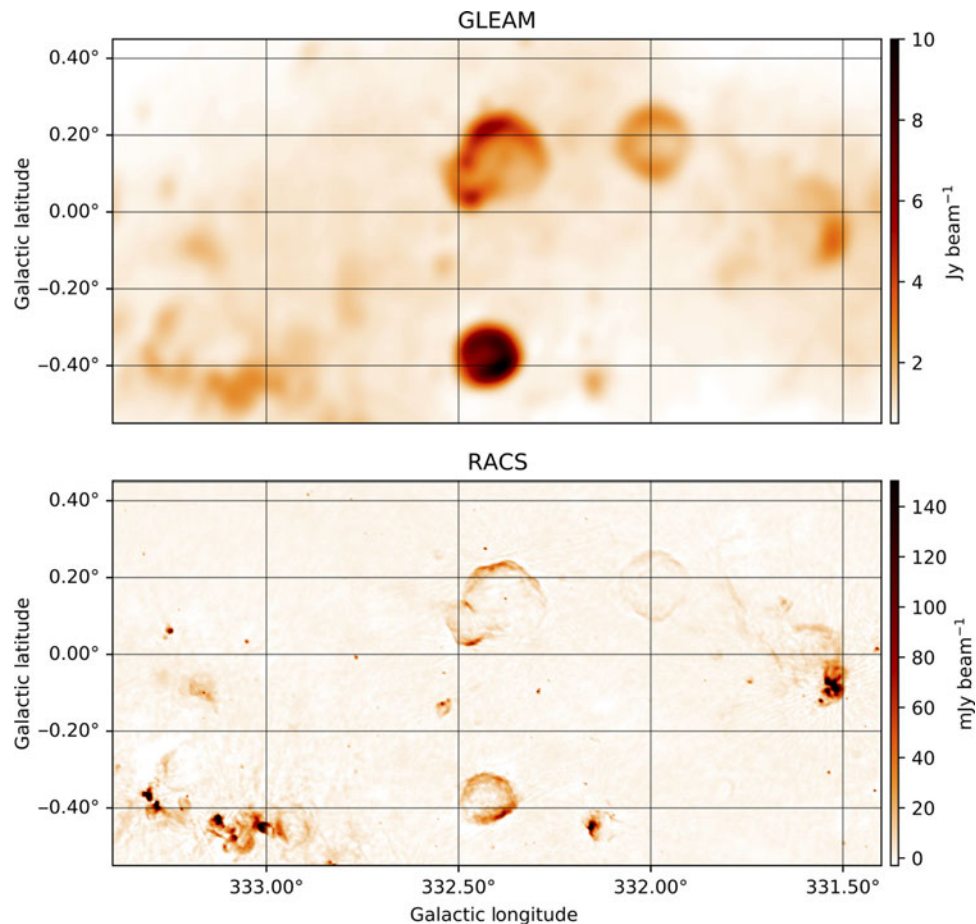
Figure 16. Images from GLEAM and RACS centred on Galactic coordinates $l = 332.3°$, $b = 0°$. This comparison illustrates the superior sensitivity of GLEAM images to large angular scales, and the finer resolution of RACS. This RACS image has a PSF size 14.5×11.5 arcsec and median image noise of 270 μJy beam^{-1}. The supernova remnants G332+0.2, G332.4 −0.4 (RCW 103), and G332.4+0.1 (MSH 16 −51, Kes 32) are prominent (cf. Whiteoak & Green 1996).

although Mercury's rapid motion required it to be tracked in phase for a proper detection.

4. RACS image release

Here we have reported on the first RACS pass over the sky in the 743.5–1031.5 MHz band. Results from this first stage of the survey are being released on CASDA as a set of data products for each of the 903 fields. Fields are named for their central J2000 position on the sky as RACS_hhmm±dd where hh, mm, and dd are each the two digits for hours and minutes of right ascension and degrees of declination, respectively. The data products released for each field are listed below:

1. Total intensity images for both the zeroth and first Taylor terms. These are approximately 7° in extent and have been brightness corrected as described in Section 3.4.4. The PSF size varies over these images so the estimation of total source flux densities requires the procedure described in Section 3.4.2 to be followed.
2. Images as for item (1) but processed to have a uniform PSF across the image.
3. Weights images, needed for proper combination of adjacent tiles.
4. Images of the image noise determined over 250-arcsec-wide cells, as introduced in Section 3.4.1.
5. Measurement sets holding calibrated visibility data, corrected for polarisation leakage at the beam centre. Note that although the visibility data for all four polarisation products (XX, XY, YX, and YY) are included, the formation of Stokes quantities (I, Q, U, V) requires knowledge of the orientation of the antennas' X and Y polarisation planes on the celestial sphere.
6. Images of the effective PSF parameters over the field of view: major and minor axes of the fitted elliptical gaussian, and its position angle. The brightness scale in each total intensity image is correct; any software tool used to estimate the integrated flux density of sources in the image will need the dimensions of the effective PSF.

All images are presented in FITS format, and the visibility data stored in CASA-style MeasurementSets.

We also make available a database[h] holding information about each field such as the circumstances of its observation and some average properties of the field image. These data are accompanied

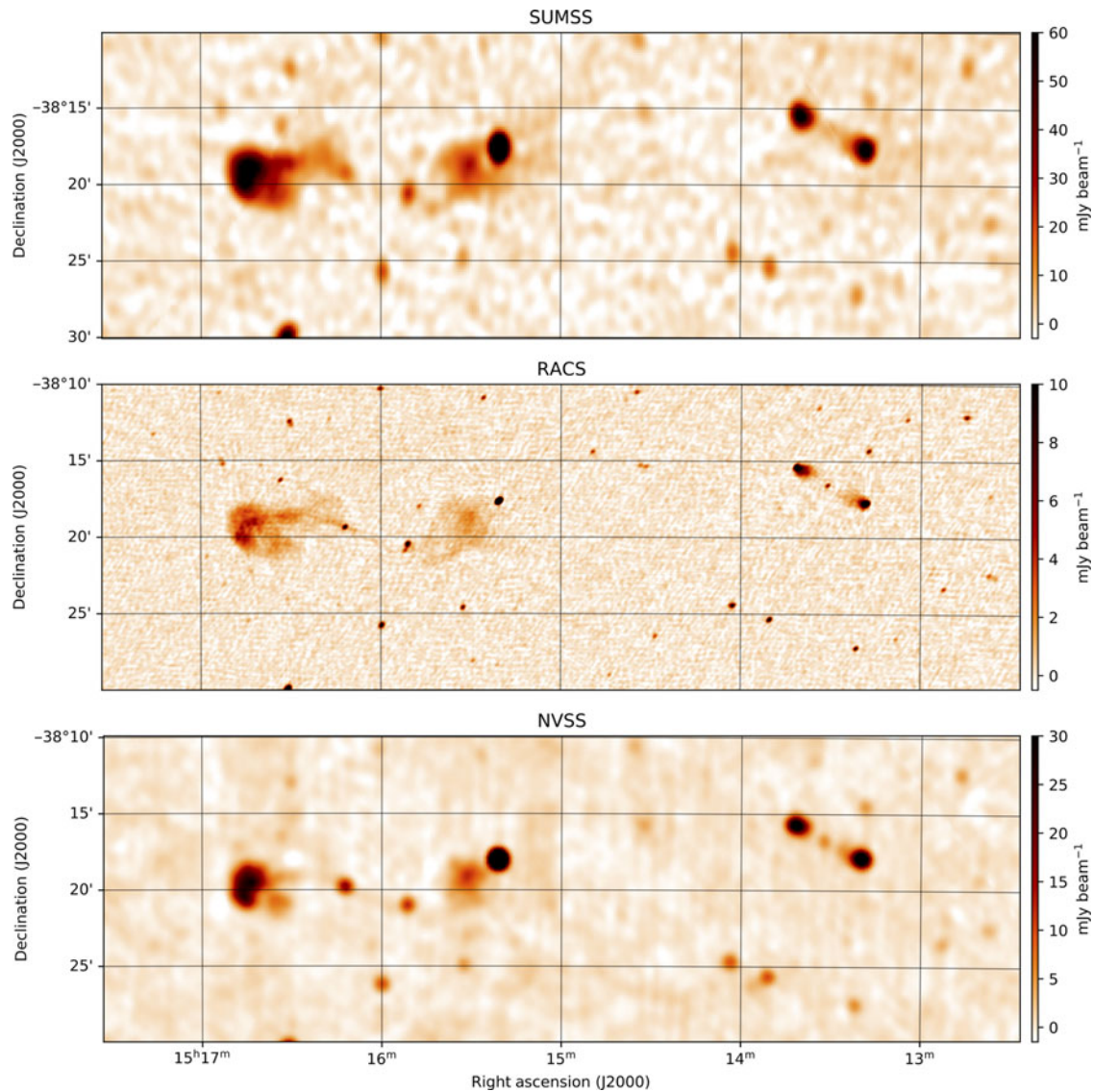[h]RACS field data base at https://bitbucket.csiro.au/projects/ASKAP_SURVEYS/repos/racs.

Figure 17. RACS, NVSS, and SUMSS images of the same region. In the RACS image, the PSF has dimensions 16 × 11 arcsec, and the image noise is 200 μJy beam^{-1}.

by software tools for accessing the database and include procedures for performing the flux density corrections mentioned above.

Additional items will be added to the CASDA release in future:

1. Additional, lower-quality images of the fields with multiple observations; these may be useful for variability studies.
2. Images of 6.3° extent, but with full sensitivity to the image boundaries. These will be prepared by linear combination with adjacent tiles.

Observations for RACS will continue, specifically to sample other parts of the spectrum accessible to ASKAP. Images from those future observations will be added to the RACS archive on CASDA.

5. Summary

We have introduced the RACS and the publication of its first total intensity images covering the whole sky south of declination +41°. In Section 3, we have characterised the performance of ASKAP during the RACS observations and have presented the corresponding properties of the survey data products. These we summarise in Table 4.

Over most of the surveyed area, the RACS images are of high quality. The low spatial frequencies in bright extended sources have been difficult to represent well, partly for lack of rotational synthesis. Data quality improved through the course of the RACS observations (2019 April to 2020 June); management of the PAFs has improved, and improved scheduling has led to more compact image PSFs.

The RACS dataset has enabled a thorough analysis of the ASKAP flux density calibration and will inform future changes to standard telescope operating procedures. Beams shapes will be measured routinely, and the results used by mosaicing software to produce images with flat flux density scale across their extent.

The images we release will provide a useful reference image of the radio sky in the 30-cm band, bridging the spectrum between low-frequency surveys such as TGSS and GLEAM and NVSS at

Table 4. Survey properties.

Number of images		903
Image size		60 deg^2
Total survey area		34240 deg^2
Repeated fields		318
Reference frequency		887.5 MHz
Bandwidth		288 MHz
Polarisation		Stokes I
Image type		MFS^a; Taylor terms 0,1
Astrometric precision	$\Delta\theta$	0.8 arcsec
Astrometric accuracy	$\Delta\alpha\cos\delta$	–0.6±0.6 arcsec
	$\Delta\delta$	–0.4±0.7 arcsec
Point spread function	B_{min}	$9.8 < 11.8 \pm 0.9 < 15.5$ arcsec
	B_{maj}	$12.0 < 18.0 \pm 4.3 < 33.1$ arcsec
Image noise	(tile medians)	$173 < 261 \pm 66 < 984\,\mu$Jy beam^{-1}

^{a}MFS = multi-frequency synthesis.

1.4 GHz. Applications will include the search for radio transients. A total intensity source catalogue is being prepared from the RACS images (RACS paper II).

RACS observations will continue at the higher ASKAP frequencies, allowing the GSM to be applicable to all ASKAP surveys.

References

Anderson, C., et al. 2018, Galaxies, 6, 127

Bondi, M., Ciliegi, P., Schinnerer, E., Smolčić, V., Jahnke, K., Carilli, C., & Zamorani, G. 2008, ApJ, 681, 1129

Briggs, D. S. 1995, PhD thesis, New Mexico Institute of Mining and Technology, http://www.aoc.nrao.edu/dissertations/dbriggs/

Bunton, J. D., & Hay, S. G. 2010, in International Conference on Electromagnetics in Advanced Applications, 728

Callingham, J. R., et al. 2017, ApJ, 836, 174

Chapman, J. M., Dempsey, J., Miller, D., Heywood, I., Pritchard, J., Sangster, E., Whiting, M., & Dart, M. 2017, in Astronomical Society of the Pacific Conference Series, Vol. 512, Astronomical Data Analysis Software and Systems XXV, ed. N. P. F. Lorente, K. Shortridge, & R. Wayth, 73

Chippendale, A., & Anderson, C. 2019, Technical report, ATNF ACES Memo 19: On-Dish Calibration of XY Phase for ASKAP's Phased Array Feeds. CSIRO

Condon, J. J. 1997, PASP, 109, 166

Condon, J. J., Cotton, W. D., Greisen, E. W., Yin, Q. F., Perley, R. A., Taylor, G. B., & Broderick, J. J. 1998, AJ, 115, 1693

Cornwell, T. J., Golap, K., & Bhatnagar, S. 2008, IEEE JSTSP, 2, 647

Cornwell, T., Humphreys, B., Lenc, E., Voronkov, M., & Whiting, M. 2011a, Technical report, ATNF ASKAP memorandum 27: ASKAP Science Processing, https://www.atnf.csiro.au/projects/askap/ASKAP-SW-0020.pdf. CSIRO, https://www.atnf.csiro.au/projects/askap/ASKAP-SW-0020.pdf

Cornwell, T., Humphreys, B., Lenc, E., Voronkov, M., & Whiting, M. 2011b, ATNF ASKAP memorandum 27, 1–67

de Gasperin, F., Intema, H. T., & Frail, D. A. 2018, MNRAS, 474, 5008

Gupta, N., Johnston, S., Feain, I., & Cornwell, T. 2008, Technical report, ATNF ASKAP Memorandum 16: The Initial Array Configuration for ASKAP, https://www.atnf.csiro.au/projects/askap/newdocs/configs-3. pdf. CSIRO, https://www.atnf.csiro.au/projects/askap/newdocs/configs-3.pdf

Guzman, J., et al. 2019, ASKAPsoft: ASKAP science data processor software, astrophysics source code library, record ascl:1912.003

Hamaker, J. P., & Bregman, J. D. 1996, AAS, 117, 161

Hotan, A. W. 2016, ACES memorandum, 11, 1

Hotan, A. W., et al. 2014, PASA, 31, e041

Hurley-Walker, N., et al. 2016, MNRAS, 464, 1146

Hurley-Walker, N., et al. 2017, MNRAS, 464, 1146

Intema, H. T., Jagannathan, P., Mooley, K. P., & Frail, D. A. 2017, A&A, 598, A78

Johnston, S., et al. 2007, PASA, 24, 174

Lacy, M., et al. 2020, PASP, 132, 035001

Lane, W. M., Cotton, W. D., van Velzen, S., Clarke, T. E., Kassim, N. E., Helmboldt, J. F., Lazio, T. J. W., & Cohen, A. S. 2014, MNRAS, 440, 327

Lenc, E., Murphy, T., Lynch, C. R., Kaplan, D. L., & Zhang, S. N. 2018, MNRAS, 478, 2835

Maggi, P., et al. 2019, A&A, 631, A127

Mauch, T., Murphy, T., Buttery, H. J., Curran, J., Hunstead, R. W., Piestrzynski, B., Robertson, J. G., & Sadler, E. M. 2003, MNRAS, 342, 1117

McConnell, D., et al. 2016, PASA, 33, e042

Murphy, T., Mauch, T., Green, A., Hunstead, R. W., Piestrzynska, B., Kels, A. P., & Sztajer, P. 2007, MNRAS, 382, 382

Perley, R. A., & Butler, B. J. 2017, The Astrophysical Journal Supplement Series, 230, 7

Rau, U. 2010, PhD thesis, New Mexico Institute of Mining and Technology, http://www.aoc.nrao.edu/~rurvashi/DataFiles/UrvashiRV_PhdThesis.pdf

Reynolds, J. 1994, ATNF Technical Memos, AT/39.3/040

Sault, R. J. 2014, Technical report, ATNF ACES Memo 2: Initial characterisation of BETA polarimetric response, https://www.atnf.csiro.au/projects/askap/Polarization_RJS_memo.pdf. CSIRO, https://www.atnf.csiro.au/projects/askap/Polarization_RJS_memo.pdf

Sault, R. J. 2015, ACES memorandum, 7, 1

Schnitzeler, D., et al. 2011, Technical report, Australia Telescope Technical memo # AT/39.9/129, https://www.atnf.csiro.au/observers/memos/AT39.9_129.pdf. CSIRO, https://www.atnf.csiro.au/observers/memos/AT39.9_129.pdf

Smolčić, V., et al. 2017, A&A, 602, A1

Wayth, R. B., et al. 2015, PASA, 32, e025

Whiteoak, J. B. Z., & Green A. J. 1996, A&AS, 118, 329

Whiting, M. T. 2012, MNRAS, 421, 3242

Whiting, M., & Humphreys, B. 2012, PASA, 29, 371

A. Computing the flux density scale corrections

Explanation of the brightness scale correction procedure justifies a brief review of linear mosaicing, the determination of sky brightness as the linear combination of brightness measures from several overlapping images. Let $B_t = B_t(l, m)$ be the true sky brightness at position (l, m). We image the sky with n beams $i = 0, ..n - 1$ and in each we measure a brightness $b_i(l, m)$, from which we estimate the measured brightness $B_m(l, m)$ as:

$$B_m = \frac{\sum_i w_i \frac{b_i}{A_i}}{\sum w_i} = \frac{\Sigma b_i A_i}{\Sigma A_i^2}, \tag{A1}$$

where A_i is the modelled amplitude of the ith beam at (l, m) $(0 \leq A_i \leq 1)$ and $w_i = w_i(l, m)$ is a direction-dependent weight. We weight each image by its inverse variance and assume that $w_i(l, m) = (\sigma_0/A_i(l, m))^{-2}$ where σ_0 has the same value for all beams. In practice, this assumption is violated, but the errors introduced in this application are typically less than 1%.

With knowledge of the true beam shapes H_i, we can write $b_i = B_t H_i$ so that, after rearrangement, an expression for the true brightness is

$$B_t = B_m \frac{\sum A_i^2}{\sum c_i H_i A_i}. \tag{A2}$$

The beams of the RACS footprint were measured using the standard holography technique (Hotan 2016) on 2020 February 6. That measurement yielded values of H for each beam on each antenna (excluding the antenna used as the holography reference) and as a function of frequency. Asymmetries in beam shape, particularly evident in beams far from the field centre, lead to the point of maximum response falling closer to the optical axis than the nominal beam centre. Consequently, the calibration source is not placed at the beam maximum, introducing an error in its inferred amplitude. The additional beam-specific term c_i included in Equation (A2) corrects for this effect and is determined from H_i in the direction of the nominal beam centre.

The expression (A2) can be calculated as a function of frequency ν: $f = B_t/B_m = f(\nu)$. This allows the determination of corrections to both the zeroth and first Taylor term images. The intensity at the imaged position in the sky is written as:

$$I_\nu = I_0 + \frac{\nu - \nu_0}{\nu_0} I_1 + \ldots \tag{A3}$$

where I_0 and I_1 are the zeroth and first Taylor-term images produced by the ASKAPsoft pipeline. Expanding $f(\nu)$ in the same way:

$$f_\nu = f_0 + \frac{\nu - \nu_0}{\nu_0} f_1 + \ldots \tag{A4}$$

allows the corrected intensity to be written as:

$$I_\nu f_\nu = \left[I_0 + \frac{\nu - \nu_0}{\nu_0} I_1 \right] \left[f_0 + \frac{\nu - \nu_0}{\nu_0} f_1 \right]$$
$$= I_0 f_0 + \frac{\nu - \nu_0}{\nu_0} [I_1 f_0 + I_0 f_1] + \ldots \tag{A5}$$

This was used to correct both the zeroth and first Taylor-term images.